RESEARCH ARTICLE

Characterising the Spatial Overlap Between Liquid and Ice in Mixed-Phase Clouds

Matthew D. Evans[1] | Steven J. Abel[1,2] | Paul R. Field[1,2] | Declan L. Finney[3] | Gary Lloyd[4] | Richard Cotton[1] | Daniel K.E. Smith[5] | Benjamin J. Murray[2] | Xinyi Huang[2]

[1]Met Office, Fitzroy Road, Exeter, EX1 3PB, UK

[2]Institute for Climate and Atmospheric Science, School of Earth and Environment, University of Leeds, Woodhouse Road, Leeds, LS2 9JT, UK

[3]National Centre for Atmospheric Science, University of Leeds, Leeds, LS2 9PH, UK

[4]Atmospheric Science Research Group, Department of Earth and Environmental Sciences, University of Manchester, Oxford Road, Manchester, M13 9PL, UK

[5]School of Environmental Sciences, University of East Anglia, Norwich, NR4 7TJ, UK

Correspondence
Matthew D. Evans, Met Office, Fitzroy Road, Exeter, EX1 3PB, UK
Email: matt.evans@metoffice.gov.uk

Funding information

Mixed-phase clouds are important for simulating precipitation formation and cloud radiative effects in Numerical Weather Prediction (NWP) and climate models. One challenge to reduce model uncertainties is how to best represent the sub-grid distribution of liquid and ice within a model grid-box. This is poorly constrained by observations, yet is key for representing microphysical process rates that grow ice crystals at the expense of liquid droplets. This study uses in-situ airborne observations from stratiform, shallow cumulus, deep convective and frontal clouds to investigate the horizontal spatial overlap of liquid and ice phases on length scales ~1 km, which are appropriate for current regional NWP models. We place observational constraints on a simple parametrisation that describes the mixed-phase fraction as a function of sub-grid liquid and ice cloud fractions and demonstrate that most of the observations show that when ice and liquid are present they are close to fully overlapped.

KEYWORDS
clouds, airborne observations, mixed-phase, parametrisation, phase overlap, cloud fractions

1 | INTRODUCTION

Mixed-phase clouds contain both supercooled liquid droplets and ice crystals. These clouds are globally widespread, appearing from the Southern Ocean (D'Alessandro et al., 2021) to the Arctic regions (Abel et al., 2017), and are challenging to simulate. Some of these challenges arise from the underestimation of supercooled liquid water (Hofer et al., 2024) which leads to uncertainties in climate change projections. The amount of liquid water in mixed-phase clouds is greatly impacted by the formation of ice crystals through primary and secondary ice production. These processes are key to the development and evolution of mixed-phase clouds. The formation of ice is highly uncertain in modelling mixed-phase clouds due to challenges in measuring and representing ice-nucleating particles (INPs) (Heymsfield et al., 2017) and ice crystal concentrations (Field et al., 2016) in primary and secondary ice production parametrisations, respectively. These modelling challenges give rise to climate model biases, such as an underestimate in the reflected short-wave radiation over the Southern Ocean, that in turn contributes to a warm sea surface temperature bias in the region (Bodas-Salcedo et al., 2014), and excessive radiative surface cooling in Arctic winter, leading to strong temperature inversions (Pithan et al., 2014).

A number of Numerical Weather Prediction (NWP) weather and climate models use ice and liquid cloud fraction schemes (Wilson et al., 2008; Van Weverberg et al., 2021), to represent the phase distribution of clouds within a model grid-box (Bogenschutz et al., 2012; Walters et al., 2019). A challenge when considering mixed-phase clouds is how to represent the degree of horizontal spatial overlap between the sub-grid liquid and ice cloud fractions, which determines the mixed-phase cloud fraction in the grid-box. Theoretical studies (Yang et al., 2014; Korolev et al., 2017) have examined the impact of the phase spatial distribution of mixed-phase clouds and it was demonstrated that the evolution of mixed-phase clouds was sensitive to microphysical processes such as riming and the Wegener-Bergeron-Findeison (WBF) process (Wegener, 1911; Bergeron, 1935; Findeisen, 1938). In the WBF process, ice crystals grow at the expense of water droplets due to a vapour pressure difference between the liquid and ice vapour pressures, and in models this process is directly proportional to the mixed-phase overlap. The WBF mechanism therefore plays an important role in the production of ice and, hence, the development and lifetime of mixed-phase clouds. In turn, this will lead to implications for precipitation rates and radiative energy balances of these clouds (Korolev and Milbrandt, 2022). Previous modelling studies have assumed maximal sub-grid overlap between liquid and ice phases (Gettelman et al., 2010; Fan et al., 2011) and this resulted in the largest possible rate of liquid depletion via the WBF mechanism. In order to shield regions of liquid water from the WBF process, other investigations have limited this horizontal overlap in model simulations. Reducing the degree of horizontal spatial overlap led to an increase in the liquid water path (LWP) of mixed-phase clouds (Abel et al., 2017).

Observational studies have used airborne measurements (Field et al., 2004; D'Alessandro et al., 2021; Korolev and Milbrandt, 2022) and active satellite based remote sensing measurements e.g. using lidar (Sokol and Storelvmo, 2024) or combinations of radar and lidar (Coopman and Tan, 2023), to examine the spatial homogeneity of mixed-phase clouds. Korolev and Milbrandt (2022) used in-situ aircraft observations of clouds over the Arctic and Canadian regions to determine the horizontal length scales of continuous ice, liquid and mixed-phase cloud segments. It was found that these lengths varied from 100 m (limited by the instrument resolution) to 100 km with high spatial phase intermittency at small length scales (~100 m). Field et al. (2004) and Korolev and Milbrandt (2022) both demonstrate that lengths of contiguous regions of mixed-phase appear to follow power law relations down to 100 m scales. Another example using in-situ airborne measurements is given by D'Alessandro et al. (2021). Here, the lengths of contiguous ice, liquid and mixed-phase sections of mixed-phase cloud regions over the Southern Ocean was determined (for length scales ~100 m–10 km) and it was found that mixed-phase regions were the shortest cloud phase segments and, hence, were the most spatially heterogeneous. The advantages of in-situ airborne observations over satellite measurements

is that they can measure individual hydrometeors, enabling finer sampling and identification of mixed-phase clouds appropriate for high-resolution, convection permitting models. However, aircraft length scales are limited, depending on the speed of the aircraft and the length of cloud sampling runs. Satellite measurements yield a global view but are limited to larger horizontal scales than can be examined with in-situ measurements. Satellite retrievals can also have difficulty detecting low concentrations of ice particles in mixed-phase clouds. For example, Coopman and Tan (2023) used radar and lidar satellite measurements to explore the spatial distribution of the thermodynamic phases in mixed-phase clouds over the Arctic and Southern Ocean regions. From the satellite retrieval of cloud phase (liquid or ice) at a pixel resolution of ~1 km, the number of liquid-ice pixel interfaces was calculated over a 1×1° (~100 km × ~100 km) area (a cloudy object). Coopman and Tan (2023) defined a mixed-phase cloud as a cloudy object that contains at least one ice pixel and one liquid pixel. A fraction was introduced to calculate the number of liquid-ice interfaces to the maximum possible number of liquid-ice interfaces over a 1° × 1° area. This fraction was used to determine the spatial heterogeneity of the mixed-phase clouds. The smaller the number of liquid-ice interfaces, the greater the spatial heterogeneity and the liquid and ice phases are less 'mixed' in the cloud. It was found that mixed-phase clouds are often heterogeneous in nature and are structured as regions of liquid droplets and regions ice crystals.

It has been identified by Abel et al. (2017) and Korolev and Milbrandt (2022) that the horizontal sub-grid overlap between the liquid and ice phases in various NWP models is poorly constrained by observations. Whilst the observations of Field et al. (2004), D'Alessandro et al. (2021), Korolev and Milbrandt (2022) and Coopman and Tan (2023) provide insights into the spatial scales of mixed-phase clouds, it is not straightforward to adapt their results into a model parametrisation of the horizontal sub-grid overlap. For a model, a conditional sampling approach is required. So, given a liquid cloud fraction and ice cloud fraction in a grid-box what is the mixed-phase cloud fraction? This study therefore applies this conditional sampling approach on in-situ airborne observations from several field campaigns, targeting a range of mixed-phase cloud types, to investigate the horizontal spatial overlap between the liquid and ice phases in mixed-phase clouds. Here we will use aircraft observations to quantify the mixed-phase fraction as a function of the ice and liquid cloud fractions over a ~1 km horizontal length scale. We will then use these observations to test a model of the horizontal mixed-phase overlap of the liquid and ice cloud fractions that is used in the Cloud and Aerosol Interacting Microphysics (CASIM) scheme and implemented in regional NWP (Field et al., 2023). The goal is to place observational constraints on a parameter (implemented in CASIM) which describes the horizontal sub-grid overlap between the liquid and ice phases. The aircraft observations are sampled on a ~1 km horizontal length scale which is a commonly used model resolution for cloud-resolving simulations such as the Met Office UK regional model (1.5 km) (Bush et al., 2023). The field campaigns chosen and instrumentation used are presented in Section 2. The observational horizontal mixed-phase overlap results are presented in Section 3 and comparisons to the horizontal mixed-phase overlap model employed by CASIM are presented in Section 4. The importance of the horizontal sub-grid overlap for process rates and potential future work is discussed in Section 5. Section 6 presents the conclusions of this study.

2 | DATA AND INSTRUMENTATION

2.1 | Field Campaigns

In-situ airborne observations taken by the Facility for Airborne Atmospheric Measurements (FAAM) BAe-146 research aircraft from four field campaigns were analysed. These included the Arctic Cold-Air Outbreak Experiment (ACAO) (Raif et al., 2024) experiment, the Resolving climate sensitivity associated with shallow mixed-phase cloud in the oceanic mid- to high latitudes (M-Phase) experiment (Huang et al., 2025), the Deep Convective Microphysics Ex-

periment (DCMEX) (Finney et al., 2024), and the Parameterizing Ice Clouds using Airborne obServationS and triple-frequency dOppler radar data (PICASSO) campaign (Kedzuf et al., 2021). This selection of field campaigns was chosen, to examine if there is any cloud regime dependence on the mixed-phase overlap. These campaigns used similar cloud physics instrumentation which was useful when assessing and comparing the cloud phase of these different cloud regimes (see Sections 2.2, 2.3 and 3.1).

The ACAO and M-Phase campaigns both targeted boundary layer clouds that formed within cold-air outbreaks (CAOs). CAOs bring cold polar air masses that flow from the sea ice over a warmer ocean, and generate strong surface fluxes of heat and moisture that are conducive to the development of mixed-phase clouds (Brümmer, 1996; Renfrew and Moore, 1999; Kolstad et al., 2009; Fletcher et al., 2016). ACAO obtained measurements in Spring 2022 to the north of Scandinavia within the Norwegian Basin and Barents Sea, and M-Phase targeted CAOs over the Labrador Sea in Autumn 2022. The cloud regimes were primarily stratiform clouds with some sampling of shallow cumulus. The contrasting seasons and locations enabled a range of CAO cloud temperatures and aerosol conditions to be sampled.

The DCMEX field campaign focussed on taking in-situ airborne microphysical, aerosol and dynamical measurements along with remote ground based measurements of deep convective cloud formation. This formation is a result of orographic convection of isolated convective clouds over the Magdalena Mountains in New Mexico, North America (Dye et al., 1989). The DCMEX measurements, undertaken in Summer 2022, enabled reliable and frequent sampling of these clouds. The datasets and background information of this project is described in Finney et al. (2024).

The PICASSO field campaign provides a useful data set which contains in-situ observations targeting mid-latitude pre- and post-frontal clouds. This campaign obtained a series airborne and ground based measurements of cirrus and mixed-phase clouds in the UK from Winter 2018 – Spring 2019. Flights that sampled regions of mixed-phase clouds were selected.

Table 1 shows some characteristics of the aforementioned field campaigns. The total horizontal length sampled by the aircraft in mixed-phase cloud conditions is also indicated.

TABLE 1 Summary of the field campaigns investigated in this study. The mixed-phase sample length is calculated from periods where the C_{mix} (see Section 3.2) calculated from the Nevzorov probe is > 0.

Field campaign	Date	Number of flights	Mixed-phase sample length	Cloud regime
ACAO	March 2022	10	1160 km	Stratiform & some shallow Cumulus
M-Phase	Oct. – Nov. 2022	15	1614 km	Stratiform & some shallow Cumulus
DCMEX	Jul. – Aug. 2022	19	375 km	Deep Convective & some Stratiform
PICASSO	Jan. 2018 – May 2019	10	3708 km	Mid-latitude frontal clouds

2.2 | Ice and Liquid Water Content Measurements

A Nevzorov probe was used to measure cloud ice and liquid water contents in all of the field campaigns. This is a constant-temperature hot-wire probe, which has two separate heated sensors for measuring the cloud total water (TWC) and liquid water (LWC) contents (Korolev et al., 1998). The TWC sensor is a deep cone version (Korolev et al., 2013) that has a better collection efficiency than earlier versions of the instrument (Korolev et al., 1998), and is designed to capture, melt and evaporate liquid drops and ice particles. The LWC sensor is a heated wire wound onto a copper rod, and liquid droplets that impinge on the wire flatten into a thin film and evaporate. Ice particles tend

to break away from the LWC sensor, with negligible heat expended compared to complete ice evaporation (Korolev et al., 2013), although a residual signal from ice particles is often measured. The bulk water content from the sensors is calculated directly from the extra electrical energy supplied that is required for the melting and evaporating processes. The baseline drift of the Nevzorov probe during the flights is corrected following the technique described in Abel et al. (2014).

Using the TWC and LWC data, the ice water content (IWC) and LWC can be calculated (Korolev et al., 1998, 2003),

$$\mathrm{IWC} = \frac{(W_{\mathrm{TWC}} - W_{\mathrm{LWC}})}{(k - \beta)} \tag{1}$$

$$\mathrm{LWC} = W_{\mathrm{LWC}} - (\beta \mathrm{IWC}) \tag{2}$$

where W_{TWC} and W_{LWC} are the total water and liquid water contents measured by the Nevzorov TWC and LWC sensors, respectively; β accounts for the residual signal of ice detected by the LWC sensor and is defined as a fraction of the IWC; k is the ratio for the difference between the specific energy used in liquid water evaporation and ice sublimation (i.e. the additional energy required to perform the sublimation process). Note that Equations (1) and (2) have been simplified from the relations given in Korolev et al. (1998) to assume collection efficiencies equal to unity as performed in previous studies (Korolev et al., 2003).

A value for k was set at 1.12 (Korolev et al., 2003). The value of β can be estimated from examining the water content measured by the liquid sensor when flying in pure ice clouds and can vary dependent on the microphysical properties of the ice particles. Korolev et al. (1998) showed measurements where β varied in the range 0.05–0.15. A fixed value of $\beta = 0.11$ has been used in prior work which examined mixed-phase cloud properties (Korolev et al., 2003). We also use a default value of $\beta = 0.11$ in this work. Examination of data from periods of the PICASSO flights with pure ice clouds showed that β varied in the range 0.05–0.2 (not shown). The sensitivity of our results due to this uncertainty in β are explored in Section 4. In addition, the Nevzorov probe data was filtered for TWC > 0.01 g m^{-3} and measurements which met this criteria was considered as in cloud regions (Korolev et al., 2003). Further sensitivity tests adjusting the TWC threshold is outlined in Table 2 and the impact on the results is shown in Section 4.

TABLE 2 Default values and sensitivity thresholds used for the Nevzorov and 2DS/CDP variables when determining cloud phase at each second.

Method	Parameter	Description	Default	Sensitivity range
Nevzorov	β	Fraction of IWC detected by LWC sensor	0.11	0.05–0.2
Nevzorov	TWC	TWC threshold to define cloud	0.01 g m^{-3}	0.005–0.02 g m^{-3}
2DS/CDP	N_{HI}	2DS ice concentration threshold to define ice	0.14 L^{-1}	0.14–1 L^{-1}
2DS/CDP	N_{CDP}	CDP drop concentration to define liquid	2 cm^{-3}	1–4 cm^{-3}

2.3 | Ice and Liquid Number Concentration Measurements

The two-dimensional stereo (2DS) probe is an optical imaging instrument used to measure particle sizes and concentrations. It consists of two orthogonal laser beams which cross in the middle of a sample volume and illuminates two 128-photodiode linear arrays. These arrays have a 10 μm pixel resolution and covers a size range of 10–1280 μm. The design of the 2DS probe along with results from various experiments are given in Lawson et al. (2006). The 2DS images particles from which a measure of particle shape, the circularity (O), is calculated. O of particles $>\sim$80 μm measured with the 2DS were classified using the measured particle perimeter P and particle area A, where $O = P^2/(4\pi A)$ (Crosier et al., 2011). The 2DS data was filtered into subcategories: high, medium and low irregular (HI, MI and LI, respectively). From experience and previous studies (Abel et al., 2017), the threshold chosen to determine the HI class of particles are particles that have a circularity larger than 1.4. Below this threshold, mis-shaped liquid droplets might be included in the statistics. In this study, HI particles were used from the 1 Hz data to identify the ice regions/particles.

The Cloud Droplet Probe (CDP) is an Optical Particle Counter which uses a focussed beam from a diode laser and detects particles through measuring the light scattered by them. The CDP measures particle concentrations and sizes in the range of 2–50 μm; the principle of operation, along with the instrument design and performance tests, is described in Lance et al. (2010). Particles measured by the CDP were used to identify liquid water regions/droplets. The number concentrations measured by the CDP are likely to be dominated by liquid droplets and contributions of small ice particles are unlikely to be significant for the mixed-phase clouds investigated in this study. This is because ice crystals are generally bigger than the CDP detectable size range (2–50 μm) and the concentration of liquid droplets $>>$ ice particles. No data was available from the PICASSO field campaign for the 2DS probe. Therefore, the 2DS/CDP analysis could not be performed for this field campaign.

2.4 | Example Data

Figure 1 shows an example time series of the IWC and LWC data obtained by the Nevzorov probe and the corresponding 2DS/CDP data measured during ACAO flight C279. This segment of data shows an aircraft profile descent through a stratiform mixed-phase cloud layer, followed by a profile ascent back through the cloud. The variation in air temperature during the aircraft profile is also shown with temperatures ranging from ~ -18 °C at cloud base to ~ -21 °C at cloud top. The Nevzorov data shows a liquid dominated cloud top region (10:44:40 UTC to 10:45:40 UTC). Lower down in the cloud, the Nevzorov probe detects ice, and ice phase precipitation is observed beneath the liquid cloud base (10:46:10 UTC to 10:47:30 UTC). During the subsequent profile ascent, another liquid dominated cloud top region is observed at the end of the time series (10:48:00 UTC to 10:48:30 UTC). The concentration of liquid drops measured with the CDP correlates well with the Nevzorov LWC measurement. In contrast, in this example, the 2DS measured ice particle concentration shows a higher number of measurements that contain ice in the time series. These discrepancies could be due to either a mis-classification of particles as ice from the 2DS imagery e.g. from out of focus particles that may contain liquid drops, or from an underestimation in the IWC measurement from the Nevzorov. However, by choosing two independent methods to detect ice and liquid in this study, we can examine the impact of the different measurement techniques on the results. For all of the aircraft datasets, measurements during turns are screened out by removing data where the aircraft rate of change of heading $\leq 1\ ^\circ s^{-1}$. The aircraft take-off and landing data are also removed from the analysis.

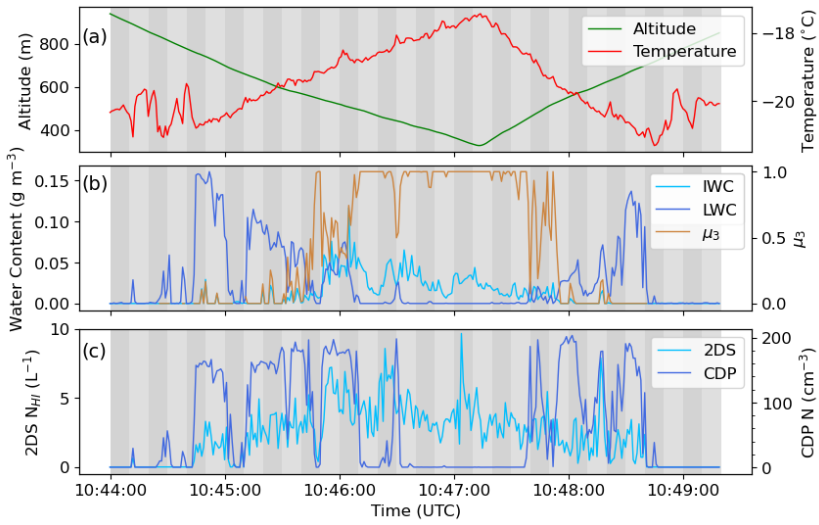

FIGURE 1 Example time series window from an ACAO flight (C279). Panel **(a)** shows the aircraft altitude and air temperature. Panel **(b)** shows IWC, LWC and μ_3 data derived from the Nevzorov probe. Panel **(c)** shows number concentration data measured by the 2DS probe and CDP. Different scales are used for the ice (2DS) and liquid (CDP) number concentrations in panel (b). The shaded grey strips represent time intervals of 10 s: for a typical aircraft true airspeed of ~100 m s^{-1}, these strips represent a distance of ~1 km.

3 | METHODOLOGY

3.1 | Determining Cloud Phase

Using the Nevzorov probe 1 Hz data, the cloud phase was determined at each second by employing the ice water content ratio (Korolev et al., 2003)

$$\mu_3 = \frac{\text{IWC}}{\text{IWC} + \text{LWC}} \tag{3}$$

where IWC and LWC are the ice and liquid water contents, respectively. Figure 1, panel (b), shows μ_3 calculated along a sample time series from an ACAO flight (C279). By applying appropriate thresholds, this ratio was used to determine different cloud phase regions: liquid cloud $(\mu_3 < 0.1)$; ice cloud $(\mu_3 > 0.9)$; and mixed-phase cloud $(0.1 \leq \mu_3 \leq 0.9)$. These phase thresholds were selected based on previous work by Korolev et al. (2003) which used Equation (3) to characterise cloud phase. Figure 2 shows a histogram of μ_3 for the CAO flights during ACAO and highlights the different phase thresholds used in this study. As found in previous studies (Korolev et al., 2003), Figure 2 highlights two maxima occurring at the pure liquid $(\mu_3 < 0.1)$ and pure ice $(\mu_3 > 0.9)$ regions. Adjustments to the β and TWC thresholds were also explored to examine the impact on the μ_3 values. Their thresholds are presented in Table 2.

An alternative technique for phase determination uses the 1 Hz data from the 2DS and the CDP. The concentration of ice particles and liquid drops are determined from the 2DS HI (N_{HI}) and the CDP (N_{CDP}) number concentration measurements respectively. Default thresholds of $N_{\text{HI}} > 0.14$ L^{-1} and $N_{\text{CDP}} > 2$ cm^{-3} were chosen to identify the ice

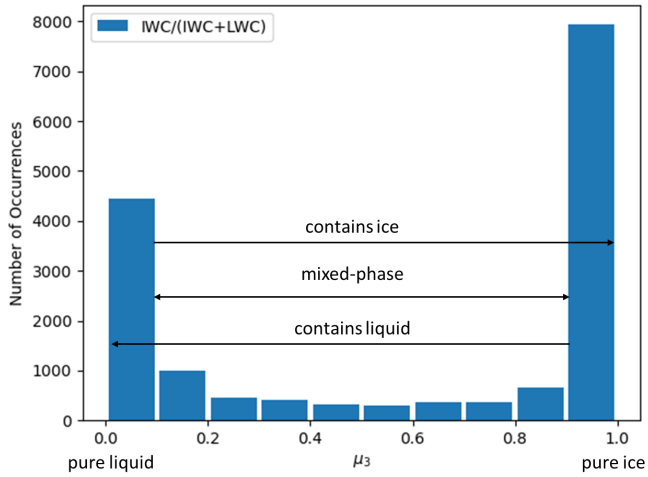

FIGURE 2 Histogram of the ratio $\mu_3 = \mathrm{IWC}/(\mathrm{LWC} + \mathrm{IWC})$ for the CAO flights during ACAO. The different thresholds used to determine cloud phase are indicated. The pure liquid $(\mu_3 < 0.1)$ and pure ice regions $(\mu_3 > 0.9)$ are labelled, along with arrows indicating regions containing some liquid $(\mu_3 \leq 0.9)$, some ice $(\mu_3 \geq 0.1)$ and mixed-phase $(0.1 \leq \mu_3 \leq 0.9)$.

and liquid water regions, respectively. Mixed-phase cloud points are calculated where both of these conditions are satisfied ($N_{\mathrm{HI}} > 0.14\ \mathrm{L}^{-1}$ and $N_{\mathrm{CDP}} > 2\ \mathrm{cm}^{-3}$). The N_{CDP} threshold ensures that out-of-cloud coarse mode aerosols are not assigned as liquid, and the N_{HI} threshold includes all ice particles measured by the 2DS (the 1 Hz detection limit of the 2DS is $0.14\ \mathrm{L}^{-1}$). The impact of increasing the default N_{HI} threshold to $1\ \mathrm{L}^{-1}$, and halving and doubling the default N_{CDP} threshold are also examined (see Table 2).

3.2 | Cloud Phase Fractions

To calculate the ice (C_{ice}), liquid (C_{liq}) and mixed-phase (C_{mix}) cloud phase fractions over aircraft sampling distances, the 1 Hz cloud-phase values were binned into 10 second time windows. This time-period corresponds to a length-scale of ~1.1 to 1.6 km based on the distance travelled by the aircraft (see Figure S1), with the range resulting from the aircraft true airspeed changing with altitude. This length scale is typical of the horizontal resolution used in many convection permitting weather forecast models e.g. the Met Office operational model over the UK has a grid-spacing of 1.5 km. The ice, liquid and mixed-phase cloud fractions are then calculated using:

$$C_{\mathrm{ice}} = \frac{\sum_{i=1}^{n} x_i}{n} \quad (x_i = 1 \ \textbf{if} \ p_i = \mathrm{Ice}; \ \ x_i = 0 \ \textbf{if} \ p_i \neq \mathrm{Ice}) \tag{4}$$

$$C_{\mathrm{liq}} = \frac{\sum_{i=1}^{n} x_i}{n} \quad (x_i = 1 \ \textbf{if} \ p_i = \mathrm{Liquid}; \ \ x_i = 0 \ \textbf{if} \ p_i \neq \mathrm{Liquid}) \tag{5}$$

$$C_{\text{mix}} = \frac{\sum_{i=1}^{n} x_i}{n} \quad (x_i = 1 \ \textbf{if} \ p_i = \text{Mixed}; \ \ x_i = 0 \ \textbf{if} \ p_i \neq \text{Mixed}) \tag{6}$$

p_i is the phase in each 1 s interval (i) and n represents the bin/time length = 10 s. Table 3 shows a summary of the (default) conditions used when determining phase, at each second, for the Nevzorov and 2DS/CDP method.

TABLE 3 Conditions and thresholds used to determine phase type, at each second, for the Nevzorov and 2DS/CDP methods. The values for the 2DS/CDP method are the default values – see Table 2 for details.

Condition	Nevzorov	2DS/CDP
p_i = Ice	$\mu_3 > 0.1$	$N_{\text{HI}} > 0.1$ L^{-1}
p_i = Liquid	$\mu_3 < 0.9$	$N_{\text{CDP}} > 2$ cm^{-3}
p_i = Mixed	$0.1 \leq \mu_3 \leq 0.9$	$N_{\text{HI}} > 0.14$ L^{-1} **and** $N_{\text{CDP}} > 2$ cm^{-3}

Figure 3 shows a time series of the cloud fractions calculated over each time window (10 s) using Equations (4), (5) and (6), and overlaid onto the example Nevzorov and 2DS/CDP data from Figure 1. The calculations from the Nevzorov in panel a) show periods of high liquid cloud fraction that are associated with a liquid dominated cloud top region, an increase in the mixed-phase cloud fraction lower down in the cloud due to the presence of both liquid and ice, and high ice cloud fractions below cloud base as the precipitation is dominated by the ice-phase. A similar pattern is shown in the liquid cloud fraction calculated from the CDP in panel b), but the ice cloud fraction calculated from the 2DS is almost always 1. This is due to the aforementioned higher frequency of ice occurrence detected by the 2DS than the Nevzorov in this example and results in time periods where the mixed-phase cloud fraction calculated from the 2DS/CDP is also larger than the Nevzorov.

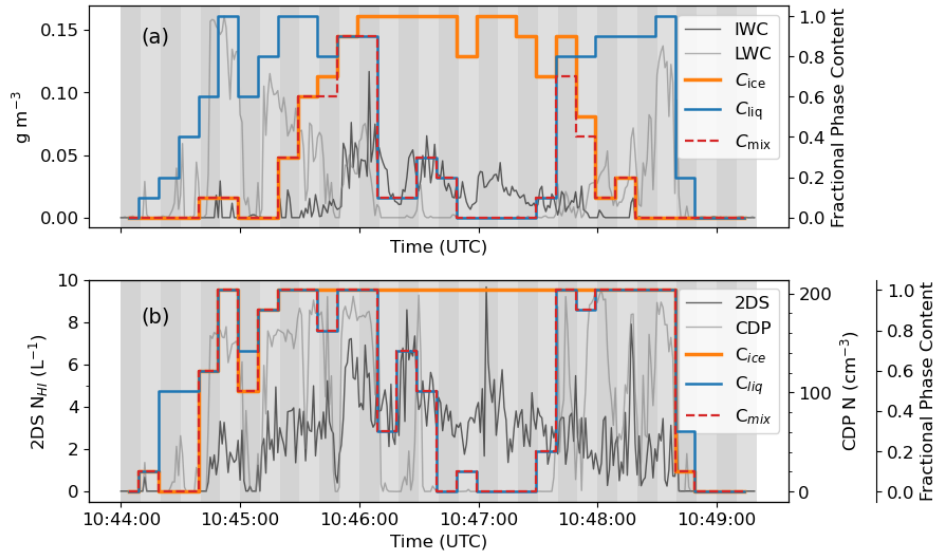

FIGURE 3 Example time series of C_{ice}, C_{liq} and C_{mix} calculated over time intervals of 10 s (~1 km grey strips) from an ACAO flight (C279). These cloud fractions are overlaid onto the **(a)** IWC and LWC data derived from the Nevzorov probe and the **(b)** number concentration data measured by the 2DS probe and CDP from Fig. 1.

4 | RESULTS

4.1 | Observations Cloud Fraction Grids

Models typically predict or diagnose ice cloud fraction and liquid cloud fraction separately. They then need to make some assumption about how much overlap there is between the two phases where mixed-phase processes can occur. Here, we use the observed cloud fractions to examine how this overlap varies as a function of the liquid and ice cloud fractions. This is achieved by constructing a two dimensional grid where C_{mix} can be binned and averaged as a function of C_{liq} and C_{ice}. This provides a useful representation of a two dimensional phase space where the resolution of these bins is determined by splitting the measured cloud fraction data into discrete 0.1 C_{liq} × 0.1 C_{ice} grid-boxes, as illustrated in Figure 4. The numbers overlaid on these observations grids show the number of individual C_{mix} observations that were binned into each grid-box. The contoured values shown in Figure 4 are the mean C_{mix} values within each grid-box from the (a) Nevzorov and (b) 2DS/CDP measurements, and use the combined data collected from all flights for every field campaign investigated in this study (as outlined in Table 1). It is interesting to note the amounts of various cloud types that are displayed. In Figure 4(a) 37% of the data points are in ice cloud ($C_{ice} > 0$, $C_{liq} = 0$), 21% are in liquid cloud ($C_{liq} > 0$, $C_{ice} = 0$), and 42% are in mixed-phase conditions ($C_{liq} > 0$ and $C_{ice} > 0$), with 15% of the mixed-phase data being in partially overcast conditions (regions where $C_{liq} < 1$ and $C_{ice} < 1$). Whereas in Figure 4(b) 49% of the data points are in ice cloud ($C_{ice} > 0$, $C_{liq} = 0$), 14% are in liquid cloud ($C_{liq} > 0$, $C_{ice} = 0$), and 37% are in mixed-phase conditions ($C_{liq} > 0$ and $C_{ice} > 0$), with 15% of the mixed-phase data being in partially overcast conditions (regions where $C_{liq} < 1$ and $C_{ice} < 1$). Figure 4(c) is a difference plot between these two grids (i.e. Figure 4(a) minus Figure 4(b)) and shows the Nevzorov method generally produces C_{mix} values higher than the 2DS/CDP grid in the partially overcast region (centre of the grid). The implications for the higher C_{mix} values calculated from

the Nevzorov method are explored further in Section 5.

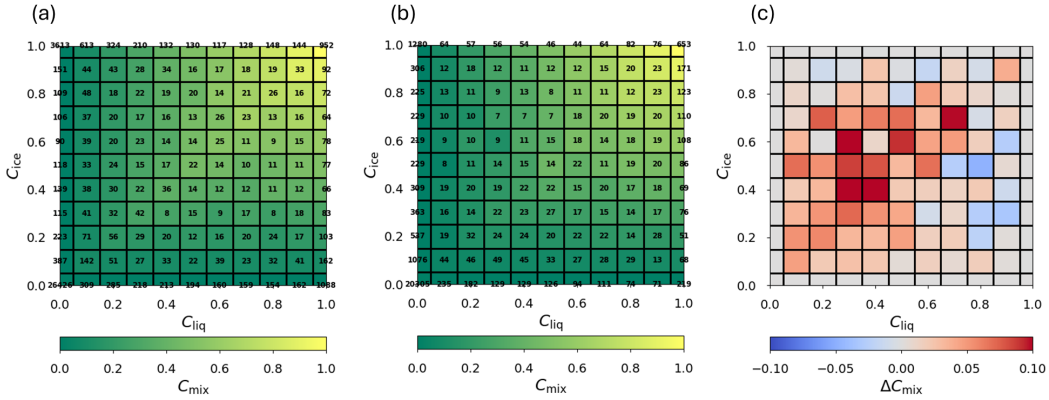

FIGURE 4 **(a)** Nevzorov and **(b)** 2DS/CDP C_{mix} grids as a function of C_{liq} and C_{ice} using the combined data collected from all flights for every field campaign investigated in this study. The printed numbers on these grids represents the number of individual C_{mix} observations per grid-box and, in this case, these are used to calculate the mean C_{mix} value in each grid-box. **(c)** is a difference plot between the Nevzorov and 2DS/CDP observations C_{mix} grid; positive regions show that the Nevzorov C_{mix} values are greater than the 2DS/CDP values. Equivalent C_{mix} grid plots for each field campaign are displayed in Figures S2, S3 and S4.

As indicated in Figure 4, each grid-box contains a number of independent C_{mix} observations. The variability in these observations is illustrated in Figure 5. The histograms show the distribution of C_{mix} values for a selection of different grid-boxes. The vertical red dashed lines in each of the histograms shows the maximum possible C_{mix} value, for each case. To examine the impact the variability in the measurements has on our results, a set of statistical properties of the C_{mix} values within each grid-box are calculated in addition to the mean: this includes the median, the interquartile range and the 10^{th} and 90^{th} percentiles of the data. Grids similar to Figure 4 can then be constructed using these additional statistical properties of the distribution for the individual grid-boxes. Example grids that illustrate this are shown in Figures S5 and S6.

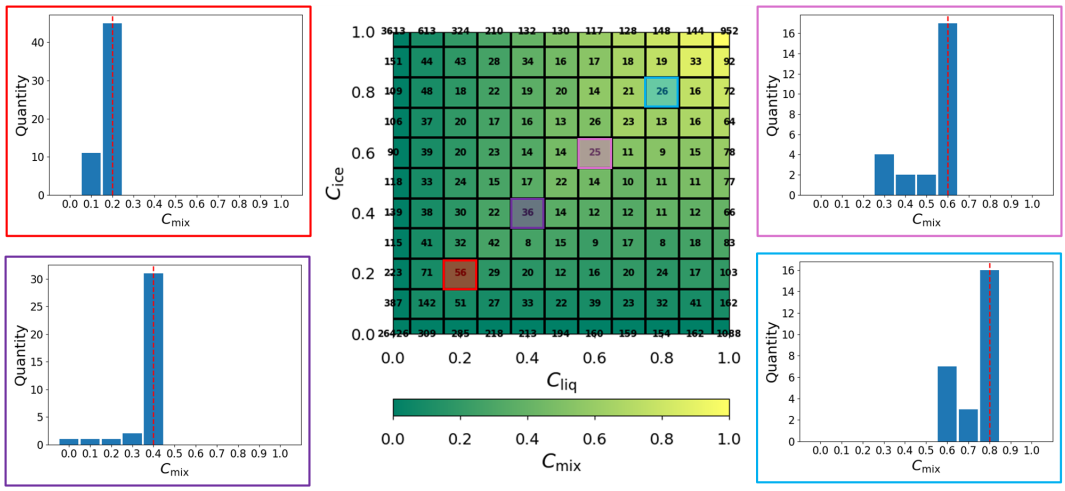

FIGURE 5 The Nevzorov C_{mix} grid, as presented in Figure 4(a), alongside histograms which show the variability of the individual observations within a selection of different grid-boxes. The red dashed vertical line indicates the maximum possible C_{mix} value in each histogram.

4.2 | Description of the Model Parametrisation

Other models may make different assumptions about how the overlap between the liquid and ice phases is done, but in CASIM it is given by this function (Field et al., 2023)

$$C_m = \text{mpof} \times \min(C_l, C_i) + \max(0, (1 - \text{mpof})(C_l + C_i - 1)) \tag{7}$$

where C_m is the model mixed-phase cloud fraction and mpof is a tunable parameter that describes the amount of sub-grid overlap between the model liquid (C_l) and model ice (C_i) cloud fractions. Note: C_m should not be misinterpreted as C_{mix}: C_m represents the model mixed-phase cloud fraction and C_{mix} is the observation mixed-phase cloud fraction. Similar to the aforementioned difference between C_m and C_{mix}, C_l and C_i are the model liquid and ice cloud fractions respectively whereas C_{liq} and C_{ice} are the observation liquid and ice cloud fractions, respectively.

The impact of varying mpof can be demonstrated by constructing a two dimensional C_m grid as a function of C_l and C_i. Figure 6 shows how the mpof parameter effects the C_m values for mpof values of 0, 0.5 and 1. It can be seen from the contours in the C_m grids that the mixed-phase cloud fraction tends to increase when increasing mpof. This is illustrated further with schematics (i)–(iv) at the bottom of Figure 6. These show how the liquid and ice cloud fractions would be distributed in a model grid-box for various combinations of C_l and C_i. Figures 6(i), 6(ii) and 6(iii) show a partially cloudy scenario whereas Figure 6(iv) shows an overcast case with higher cloud phase fractions than the aforementioned schematics. The mixed-phase cloud fraction C_m is represented by regions where C_l and C_i overlap. It is clear that as mpof increases from 0 to 1, the overlap between ice and liquid increases. The largest change in C_m between the various mpof values occurs when the grid-box is partially cloudy (Figures 6(i), 6(ii) and 6(iii)), and as the grid-box becomes more overcast the change with mpof becomes smaller (Figures 6(iv)). This is shown further in Figure S7 which plots the difference between the C_m grids using a value of mpof = 1 and mpof = 0. This highlights the area in the centre of the grid, which represents partially cloudy grid-boxes, and exhibits the largest sensitivity to

mpof.

Figure 4(c) shows that the two observation techniques are also most different in the centre of the C_{mix} grid. Furthermore, around the edges of the grid in Figure 4(c) we can see that there is no difference: these are either single phase regions where there is no mixed-phase component (bottom and far left regions of the grid), or overcast regions in mixed-phase conditions where $C_{ice} = 1$ or $C_{liq} = 1$ (top and far right of grid, respectively). Here, C_{mix} cannot change from the minimum value of C_{ice} or C_{liq}. Other grids similar to Figure 4 were produced for the individual field campaigns (Figures S2, S3 and S4) and they show the higher mean C_{mix} produced from the Nevzorov observations are common across the field campaigns.

The default value in the CASIM microphysics scheme is mpof = 0.5. This value is not constrained by observations and is simply chosen because it lies between the minimum and maximum value of mpof.

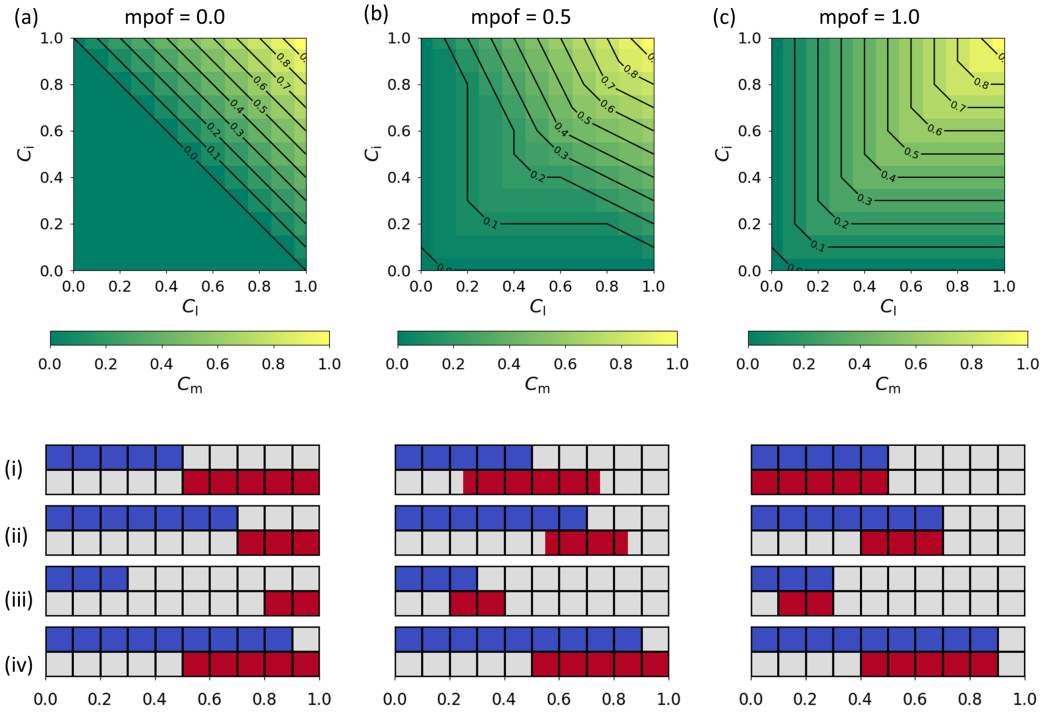

FIGURE 6 Schematic of the mixed-phase overlap parametrisation used in CASIM. From left to right, the columns show results using: **(a)** mpof = 0.0; **(b)** mpof = 0.5; **(c)** mpof = 1.0. The bottom panels show four example schematics for how the liquid (blue boxes) and ice (red boxes) cloud fractions would be distributed in the horizontal in a grid-box, corresponding to these different mpof values: **(i)** $C_l = 0.5$, $C_i = 0.5$; **(ii)** $C_l = 0.7$, $C_i = 0.3$; **(iii)** $C_l = 0.3$, $C_i = 0.2$; **(iv)** $C_l = 0.9$, $C_i = 0.5$.

4.3 | Observations and Model Parametrisation Comparison

The observations and the CASIM parametrisation can then be compared by finding the mean-squared error (MSE) between the observations grid and the CASIM parametrisation grid (e.g. Figure 6). For a fixed value of mpof:

$$MSE = \frac{\sum_{i=1}^{N} (C_{\mathrm{mix}_i} - C_{\mathrm{m}_i})^2}{N} \tag{8}$$

where the subscript i denotes an individual grid-box in the grids, C_{mix_i} is a property of the observations mixed-phase cloud fraction (e.g. the mean, median or percentile) calculated in each grid-box, C_{m_i} is the corresponding model mixed-phase cloud fraction in each CASIM parametrisation grid-box, and N is the number of grid-boxes that contain observations. The best-fit mpof between the observations and the parametrisation can then be determined from the value of mpof that produces the lowest MSE.

Figure 7(a) shows the MSE between the Nevzorov observations and the CASIM parametrisation grids as a function of mpof. The results are calculated using the mean C_{mix} value in each of the observations grid-boxes for the ACAO, M-Phase, DCMEX, PICASSO and combined datasets from the different field campaigns (Table 1). The marker for the mpof with the minimum MSE for each campaign is in the corresponding box plot. The sensitivity of the best-fit mpof that results from changing the assumptions used to calculate cloud phase from the observations (see Table 2) are shown by the shaded regions. This includes changing the value of β and the TWC threshold for the Nevzorov processing and provides a measure of the instrument uncertainty. The sensitivity of the best-fit mpof that results from the variability in the observations C_{mix} dataset within each grid-box (see Figure 5) is shown with the box-and-whiskers. These show the best-fit mpof derived using the median (vertical line), the interquartile range (boxes) and the 10^{th} to 90^{th} percentiles (whiskers) of the observations C_{mix} values in each grid-box (see Figure S5), instead of the mean value that was used in the plotted curves. Figure 7(b) shows the corresponding results from the 2DS/CDP observations. In this case, the measure of the instrument uncertainty shown with the shaded regions indicates how the best-fit mpof varies with the different N_{HI} and N_{CDP} thresholds used to define ice and liquid from the 2DS and CDP (see Table 2).

The mpof values derived from observations presented in Figure 7 show that the mpof is higher than the default value used in CASIM. The tests to examine how sensitive the derived mpof was to assumptions used in the calculation of cloud phase from the aircraft observations (shaded regions in Figures 7(a) and 7(b)) is relatively small. The tests to explore the observed variability in mpof, by using the interquartile range and 10^{th} to 90^{th} percentiles of the C_{mix} observations in each grid-box, is larger and indicates that mpof does vary in nature. But the large majority of observations still indicate an mpof value > 0.5. This suggests there is a greater degree of overlap between the liquid and ice phases than what is currently assumed in CASIM, when both liquid and ice are present in the same grid-box.

Table 4 summarises the derived mpof values for each field campaign from the Nevzorov and 2DS/CDP methods. The derived mpof using the mean, median and 10^{th} to 90^{th} percentiles (shown in parenthesis) C_{mix} values in the observations grid are shown. To highlight the greatest spread in the derived mpof values, only the variability in the observations is shown. This also encompasses the range in mpof calculated from sensitivity tests that explored uncertainties in the determination of cloud phase from the observations/instrumentation. As seen from Table 4, the biggest spread in the derived mpof is from the combined field campaign analysis. This is because there are more independent observations included in this analysis which leads to greater variability in the observations and thus yields more spread for the 10^{th} and 90^{th} percentiles of the dataset.

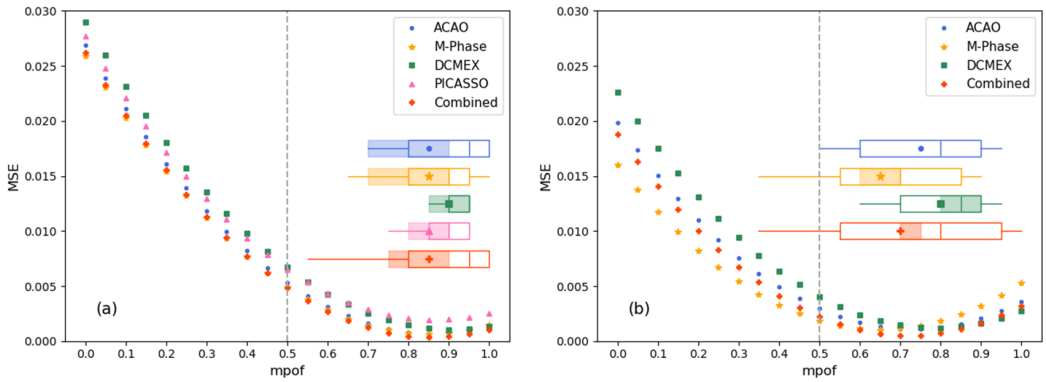

FIGURE 7 *MSE* between the observations and the CASIM parametrisation as a function of mpof. Results are shown for the **(a)** Nevzorov and **(b)** 2DS/CDP observations for the ACAO, M-Phase, DCMEX, PICASSO and combined field campaigns. Both panels show the *MSE* curves calculated using the mean C_{mix} values in the observation grid. The marker for the mpof with the minimum MSE for each campaign is in the corresponding box plot. The variability in the best-fit from the instrument uncertainty is shown by the shaded regions. See Table 2 for details. The box-and-whiskers provide a measure of the variability in the observations calculated using the median (vertical line), the interquartile range (box) and the 10th and 90th percentiles (whiskers) of the C_{mix} values in the observation grid. In both panels, the grey dashed vertical line shows the default mpof value (0.5) currently used in CASIM.

TABLE 4 Nevzorov and 2DS/CDP derived mpof for each field campaign. Results are shown for calculations that use the mean, the median and the 10th to 90th percentiles of the observations within each cloud fraction (C_{mix}) grid-box.

	Nevzorov		2DS/CDP	
Campaign	**Mean**	**Median (10th – 90th)**	**Mean**	**Median (10th – 90th)**
ACAO	0.85	0.95 (0.70 – 1.0)	0.75	0.80 (0.50 – 0.95)
M-Phase	0.85	0.90 (0.65 – 1.0)	0.65	0.70 (0.35 – 0.90)
DCMEX	0.90	0.90 (0.85 – 0.95)	0.80	0.85 (0.60 – 0.95)
PICASSO	0.85	0.90 (0.75 – 0.95)	-	-
Combined	0.85	0.95 (0.55 – 1.0)	0.70	0.80 (0.35 – 1.0)

5 | DISCUSSION

This study differs from the previous observational approaches mentioned in Section 1 by focussing on how to represent the overlap of liquid and ice phases in a model grid-box. This is of great importance for models representing the physics of clouds. Liquid amounts and fraction can be diagnosed on the basis of thermodynamic environment and, although more difficult, the presence of ice can also be predicted. However, we don't have a physically based representation of how to describe this overlap in models. To address this gap, aircraft instrumentation (i.e., Nevzorov probe and 2DS/CDP) was used in this study to determine cloud phase, where data resolution was limited to ~100 m. These cloud phase measurements were then employed to calculate cloud fractions over ~1 km length scales, which

is comparable to typical grid-box resolutions used in convection permitting NWP models. Whilst we have analysed cloud phase measurements over ~1 km length scales others have explored larger length scales using satellite observations as outlined in Section 1. Interestingly, the aforementioned investigations described in Section 1, which used both in-situ aircraft (D'Alessandro et al., 2021; Korolev and Milbrandt, 2022) and satellite (Coopman and Tan, 2023) measurements, found that the cloud phases in mixed-phase clouds tend to be organised as pockets of liquid and ice phases, rather than being uniformly mixed. It was noted by Coopman and Tan (2023) that the degree of phase spatial distribution is affected by other factors: higher temperatures are associated with homogeneously mixed mixed-phase clouds and higher concentrations of black carbon are associated with heterogeneously mixed mixed-phase clouds. This suggests other physical parameters (such as temperature and vertical velocity) will affect the degree of overlap. Indeed, Korolev (2008) theoretically showed that temperature, pressure, vertical velocity and integral radii play an important role in the phase transformations in mixed-phase clouds. Although we have no physical laws to govern the phase overlap, the work presented in this study provides an empirical dataset to test model assumptions. From Figure 5 it is clear that the C_{mix} is skewed towards its maximum possible value. This indicates that, when ice and liquid are present in km-scale regions, they tend towards being maximally overlapped.

Comparison of the observations analysed in this study to the mixed-phase fraction model used in CASIM shows that the liquid and ice phases tend to be have a greater degree of overlap than what is currently used in CASIM. This is shown from the MSE as a function of mpof investigations in Section 4. Figures 7(a) and 7(b) both show that the mpof minima/best-fit values derived from the mean C_{mix} observation grid values are greater than the CASIM (0.5) default value. Although the best-fit mpof values in Figure 7 are greater than the CASIM default value, it should be noted that there is spread associated with the derived mpof values when uncertainties from the variable observation datasets and instrumentation thresholds are considered. This is especially evident when considering the impact of the variability in the measured cloud segments from the observations datasets as presented by the box-and-whiskers plots in Figures 7(a) and 7(b). The results in Figure 7(b) show there is little sensitivity to the instrument uncertainty arising from adjustments in the N_{HI} and N_{CDP} threshold values. However, Figure 7(a) indicates a greater sensitivity in the derived mpof results to the Nevzorov instrument uncertainty which originates from adjustments to the TWC and β thresholds. These sources and amounts of variability are important to acknowledge; this highlights that the overlap between the liquid and ice phases does indeed vary in mixed-phase clouds. By analysing data obtained from two different sets of instruments, the robustness and validity of the derived mpof results are improved. Even though there is more spread in the best-fit mpof values (0.65–0.80) from the 2DS/CDP method compared to the Nevzorov method (0.85–0.90), the mpof values derived from both instrument methods are greater than the current CASIM (0.5) value. It should be noted that the derived mpof values in Figure 7(a) from the Nevzorov method are higher than those derived from the 2DS/CDP method in Figure 7(b). To understand this, Figure 4(c) shows the difference plot between the Nevzorov and 2DS/CDP combined field campaign data observation C_{mix} grids. This highlights the Nevzorov method produces higher C_{mix} values than the 2DS/CDP method in the centre of the C_{mix} grid. This region of the grid, which represents partially cloudy grid-boxes, exhibits the largest sensitivity to mpof in the model parameterisation (see Figure 6 and Figure S7). Therefore, the higher C_{mix} values in the centre of the Nevzorov observation C_{mix} grids will lead to a higher derived mpof value, as predicted by Equation 7.

If a value of mpof > 0.5 is used in CASIM, this would result in a greater degree of sub-grid overlap between the liquid and ice phases and would lead to the enhancement of microphysical process rates, such as the WBF mechanism and riming. These enhanced processes would increase the rate at which ice crystals grow at the expense of liquid droplets and lead to the glaciation of mixed-phase clouds. Subsequently, this decreases the lifetime of mixed-phase regions, increases precipitation rates and alters radiation balances. An example that explores the impact of changing the degree of overlap for mixed-phase boundary layer clouds in a cold-air outbreak sampled during the M-Phase

campaign is shown in Figure S8. For this case-study, increasing mpof in the CASIM scheme from 0.5 to 0.9 decreased both the cloud liquid water path by 11 g m^{-2} (12%) and the outgoing short-wave top-of-atmosphere flux by 4 W m^{-2} (2%) averaged over the region sampled by the aircraft. A further example is given in Smith et al. (2025), who performed sensitivity tests that implemented minimal (mpof = 0) and maximal (mpof = 1.0) overlap in modelling studies for low-level and frontal mixed-phase clouds over the Southern Ocean. When mpof was increased, the amount of liquid water in these clouds was reduced as a result of the enhancement of the WBF mechanism and riming process. Subsequently, Smith et al. (2025) showed that the radiative properties of these clouds exhibited a large sensitivity to mpof and revealed this sensitivity was due to the albedo being lowered as a result of the amount of liquid water in these clouds being reduced (via cloud glaciation) as the mpof is increased. Different studies which explored boundary layer cloud modelling from CAOs identified models typically underestimate the liquid cloud fraction in cumulus clouds from CAOs (Zheng et al., 2024). Other investigations have separated the ice and liquid to compensate for the rapid liquid depletion from ice due to the WBF and riming processes (Abel et al., 2017). The results presented in Section 4 indicate the liquid and ice phases in mixed-phase clouds are more overlapped than what is currently assumed in CASIM. Therefore, other model processes (such as too much primary ice production and/or too much secondary ice production) may need to be investigated to address the rapid depletion of supercooled liquid water (or LWP) in Met Office regional modelling systems.

For the campaigns investigated, it was found there was little sensitivity to the cloud regime studied. This means a single value of mpof could be selected to be implemented in the CASIM scheme. It should be noted that not all possible types of cloud regime were investigated and, to explore this choice further, this analysis could be extended to incorporate other cloud regimes for different regions across the globe.

6 | CONCLUSIONS

This study uses aircraft observations of ice and liquid water contents from the Nevzorov probe in addition to ice and liquid number concentrations from the 2DS/CDP to assess the mixed-phase cloud fraction in ~1 km regions as a function of ice and liquid sub-grid cloud fraction. Using the analysed observations from a range of cloud regimes, observational constraints can be applied to a parameter used in the parametrization of mixed-phase fraction in the new CASIM cloud microphysics scheme. This parameter (mpof) varies the degree of overlap between liquid and ice in a model grid-box, and can vary from a value of 0 (minimum overlap) to 1 (maximum overlap) as illustrated in Figure 6.

The majority of the aircraft observations show that when ice and liquid are present in ~1 km regions then they are close to maximally overlapped. For models with no explicit representation of mixed-phase fraction, setting the sub-grid liquid and ice phases to be fully overlapped would be a better approximation at km-scale than minimal overlap. For the mixed-phase cloud fraction function in CASIM based on ice and liquid cloud fractions, there is a greater degree of overlap than what is currently used in CASIM (mpof = 0.50). Combined field campaign measurements obtained from the Nevzorov probe mean C_{mix} grid-box values found mpof ~ 0.85. Whereas, the combined campaign measurements using the mean C_{mix} grid-box values from the 2DS/CDP method found a slightly lower value of mpof ~ 0.70. Even though there are slight differences in the derived mpof between the two methods, both values are greater than the default one currently used in CASIM. Ideally, it would be useful to predict mpof based on some physical parameter which is perhaps linked to cloud regime, sub-grid turbulence or other variables outlined in Korolev (2008). However, in the model one number for mpof is used. Therefore, depending on the technique used (ice and liquid water contents or number concentrations), a value for mpof can be selected in the range 0.70–0.85 (Section 4, Figure 7). Selecting

an mpof value in this range would be a more suitable choice at representing the spatial sub-grid overlap of liquid and ice than the current (mpof = 0.50) value used in CASIM.

Altering the degree of spatial sub-grid overlap between liquid and ice will impact model simulations of various cloud microphysical process rates. In particular, this will lead to the enhancement of processes where ice crystals grow at the expense of surrounding liquid droplets such as the WBF mechanism. This will have implications for cloud development and will cause changes in the precipitation rates and radiative properties of mixed-phase clouds for future Met Office regional model simulations.

Data Availability

Field campaign flight data from the FAAM aircraft is stored on the CEDA archive:
ACAO `https://catalogue.ceda.ac.uk/uuid/01021a90c0c2481c909bdb145cb72398/`;
M-Phase `https://catalogue.ceda.ac.uk/uuid/6d7971a92d154bb29af3167dfb6f5a7e/`;
DCMEX `https://catalogue.ceda.ac.uk/uuid/b1211ad185e24b488d41dd98f957506c/`;
PICASSO `https://catalogue.ceda.ac.uk/uuid/400efba73c1d40c78f44918429ce9c99/`.
Cloud phase fractions calculated from Nevzorov and 2DS/CDP observations used for the analysis in this paper can be found at `https://doi.org/10.5281/zenodo.14526275`.

Author Contributions

The idea was conceptualised by MDE, SJA, PRF and DLF. Research flights were planned and conducted by SJA, PRF, DLF, RJC and BJM. MDE performed the analysis and led the writing of the paper with contributions from SJA, PRF and DLF. SJA, RJC and MDE processed the Nevorov data. GL processed the data and imagery from the 2DS probe. DKES provided useful discussions throughout the project. XH provided the example model case study. All authors reviewed the manuscript.

Acknowledgements

The airborne data was collected using the FAAM BAe-146-301 Atmospheric Research Aircraft, flown by Airtask Ltd., maintained by Avalon Aero Ltd. and managed by FAAM Airborne Laboratory. The FAAM Airborne Laboratory's research aircraft is owned by UK Research and Innovation (UKRI) and the Natural Environmental Research Council (NERC). It is managed through the National Centre for Atmospheric Science, and leased through the University of Leeds. We are grateful to all of the people from the Met Office, the University of Leeds, University of Manchester, FAAM, Airtask and Avalon Aero that were instrumental in making the research flights from the various field campaigns a success. Alan Blyth is thanked for his significant contribution to DCMEX and making the field campaign a success. Jonathan Crosier and Chris Westbrook are thanked for their significant contributions to the PICASSO field campaign and making this a success. The Mission Scientists involved with the various field campaigns are thanked for collecting the data during research flights. The ACAO flight campaign was largely funded by the Met Office, with a contribution of additional flight hours from M-Phase. M-Phase and DCMEX were supported by NERC as part of the CloudSense Programme (M-Phase: NE/T00648X/1 and NE/T006463/1; and DCMEX: NE/T006420/1 and NE/T006439/1). PICASSO was funded by NERC under the grant number NE/P012426/1. Daniel Smith was funded by the project grant number NE/T006404/1. Ian Renfrew is thanked for the useful discussions around this project.

Conflict of Interest

The authors declare that they have no conflict of interest.

references

Abel, S. J., Boutle, I. A., Waite, K., Fox, S., Brown, P. R. A., Cotton, R., Lloyd, G., Choularton, T. W. and Bower, K. N. (2017) The Role of Precipitation in Controlling the Transition from Stratocumulus to Cumulus Clouds in a Northern Hemisphere Cold-Air Outbreak. *Journal of the Atmospheric Sciences*, **74**, 2293–2314. URL: https://journals.ametsoc.org/doi/10.1175/JAS-D-16-0362.1.

Abel, S. J., Cotton, R. J., Barrett, P. A. and Vance, A. K. (2014) A comparison of ice water content measurement techniques on the FAAM BAe-146 aircraft. *Atmospheric Measurement Techniques*, **7**, 3007–3022. URL: https://amt.copernicus.org/articles/7/3007/2014/.

Bergeron, T. (1935) *On the physics of clouds and precipitation. In Proces Verbaux de l'Association de Météorologie*. International Union of Geodesy and Geophysics.

Bodas-Salcedo, A., Williams, K. D., Ringer, M. A., Beau, I., Cole, J. N. S., Dufresne, J.-L., Koshiro, T., Stevens, B., Wang, Z. and Yokohata, T. (2014) Origins of the Solar Radiation Biases over the Southern Ocean in CFMIP2 Models*. *Journal of Climate*, **27**, 41–56. URL: http://journals.ametsoc.org/doi/10.1175/JCLI-D-13-00169.1.

Bogenschutz, P. A., Gettelman, A., Morrison, H., Larson, V. E., Schanen, D. P., Meyer, N. R. and Craig, C. (2012) Unified parameterization of the planetary boundary layer and shallow convection with a higher-order turbulence closure in the Community Atmosphere Model: single-column experiments. *Geoscientific Model Development*, **5**, 1407–1423. URL: https://gmd.copernicus.org/articles/5/1407/2012/.

Brümmer, B. (1996) Boundary-layer modification in wintertime cold-air outbreaks from the Arctic sea ice. *Boundary-Layer Meteorology*, **80**, 109–125. URL: http://link.springer.com/10.1007/BF00119014.

Bush, M., Boutle, I., Edwards, J., Finnenkoetter, A., Franklin, C., Hanley, K., Jayakumar, A., Lewis, H., Lock, A., Mittermaier, M., Mohandas, S., North, R., Porson, A., Roux, B., Webster, S. and Weeks, M. (2023) The second Met Office Unified Model–JULES Regional Atmosphere and Land configuration, RAL2. *Geoscientific Model Development*, **16**, 1713–1734. URL: https://gmd.copernicus.org/articles/16/1713/2023/.

Coopman, Q. and Tan, I. (2023) Characterization of the Spatial Distribution of the Thermodynamic Phase Within Mixed-Phase Clouds Using Satellite Observations. *Geophysical Research Letters*, **50**, e2023GL104977. URL: https://agupubs.onlinelibrary.wiley.com/doi/10.1029/2023GL104977.

Crosier, J., Bower, K. N., Choularton, T. W., Westbrook, C. D., Connolly, P. J., Cui, Z. Q., Crawford, I. P., Capes, G. L., Coe, H., Dorsey, J. R., Williams, P. I., Illingworth, A. J., Gallagher, M. W. and Blyth, A. M. (2011) Observations of ice multiplication in a weakly convective cell embedded in supercooled mid-level stratus. *Atmospheric Chemistry and Physics*, **11**, 257–273. URL: https://acp.copernicus.org/articles/11/257/2011/.

D'Alessandro, J. J., McFarquhar, G. M., Wu, W., Stith, J. L., Jensen, J. B. and Rauber, R. M. (2021) Characterizing the Occurrence and Spatial Heterogeneity of Liquid, Ice, and Mixed Phase Low-Level Clouds Over the Southern Ocean Using in Situ Observations Acquired During SOCRATES. *Journal of Geophysical Research: Atmospheres*, **126**, e2020JD034482. URL: https://agupubs.onlinelibrary.wiley.com/doi/10.1029/2020JD034482.

Dye, J. E., Winn, W. P., Jones, J. J. and Breed, D. W. (1989) The electrification of New Mexico thunderstorms: 1. Relationship between precipitation development and the onset of electrification. *Journal of Geophysical Research: Atmospheres*, **94**, 8643–8656. URL: https://agupubs.onlinelibrary.wiley.com/doi/10.1029/JD094iD06p08643.

Fan, J., Ghan, S., Ovchinnikov, M., Liu, X., Rasch, P. J. and Korolev, A. (2011) Representation of Arctic mixed-phase clouds and the Wegener-Bergeron-Findeisen process in climate models: Perspectives from a cloud-resolving study. *Journal of Geophysical Research*, **116**, D00T07. URL: http://doi.wiley.com/10.1029/2010JD015375.

Field, P. R., Hill, A., Shipway, B., Furtado, K., Wilkinson, J., Miltenberger, A., Gordon, H., Grosvenor, D. P., Stevens, R. and Van Weverberg, K. (2023) Implementation of a double moment cloud microphysics scheme in the UK met office regional numerical weather prediction model. *Quarterly Journal of the Royal Meteorological Society*, **149**, 703–739. URL: https://rmets.onlinelibrary.wiley.com/doi/10.1002/qj.4414.

Field, P. R., Hogan, R. J., Brown, P. R. A., Illingworth, A. J., Choularton, T. W., Kaye, P. H., Hirst, E. and Greenaway, R. (2004) Simultaneous radar and aircraft observations of mixed-phase cloud at the 100 m scale. *Quarterly Journal of the Royal Meteorological Society*, **130**, 1877–1904. URL: https://rmets.onlinelibrary.wiley.com/doi/10.1256/qj.03.102.

Field, P. R., Lawson, R. P., Brown, P. R. A., Lloyd, G., Westbrook, C., Moisseev, D., Miltenberger, A., Nenes, A., Blyth, A., Choularton, T., Connolly, P., Buehl, J., Crosier, J., Cui, Z., Dearden, C., DeMott, P., Flossmann, A., Heymsfield, A., Huang, Y., Kalesse, H., Kanji, Z. A., Korolev, A., Kirchgaessner, A., Lasher-Trapp, S., Leisner, T., McFarquhar, G., Phillips, V., Stith, J. and Sullivan, S. (2016) Chapter 7. Secondary Ice Production - current state of the science and recommendations for the future. *Meteorological Monographs*, AMSMONOGRAPHS–D–16–0014.1. URL: https://journals.ametsoc.org/doi/10.1175/AMSMONOGRAPHS-D-16-0014.1.

Findeisen, W. (1938) Die kolloidmeteorologischen Vorgänge bei der Niederschlagsbildung. *Meteorologiche Zeitschrift*, **55**, 121–133.

Finney, D. L., Blyth, A. M., Gallagher, M., Wu, H., Nott, G. J., Biggerstaff, M. I., Sonnenfeld, R. G., Daily, M., Walker, D., Dufton, D., Bower, K., Böing, S., Choularton, T., Crosier, J., Groves, J., Field, P. R., Coe, H., Murray, B. J., Lloyd, G., Marsden, N. A., Flynn, M., Hu, K., Thamban, N. M., Williams, P. I., Connolly, P. J., McQuaid, J. B., Robinson, J., Cui, Z., Burton, R. R., Carrie, G., Moore, R., Abel, S. J., Tiddeman, D. and Aulich, G. (2024) Deep Convective Microphysics Experiment (DCMEX) coordinated aircraft and ground observations: microphysics, aerosol, and dynamics during cumulonimbus development. *Earth System Science Data*, **16**, 2141–2163. URL: https://essd.copernicus.org/articles/16/2141/2024/.

Fletcher, J., Mason, S. and Jakob, C. (2016) The Climatology, Meteorology, and Boundary Layer Structure of Marine Cold Air Outbreaks in Both Hemispheres*. *Journal of Climate*, **29**, 1999–2014. URL: http://journals.ametsoc.org/doi/10.1175/JCLI-D-15-0268.1.

Gettelman, A., Liu, X., Ghan, S. J., Morrison, H., Park, S., Conley, A. J., Klein, S. A., Boyle, J., Mitchell, D. L. and Li, J. F. (2010) Global simulations of ice nucleation and ice supersaturation with an improved cloud scheme in the Community Atmosphere Model. *Journal of Geophysical Research: Atmospheres*, **115**, 2009JD013797. URL: https://agupubs.onlinelibrary.wiley.com/doi/10.1029/2009JD013797.

Heymsfield, A. J., Krämer, M., Luebke, A., Brown, P., Cziczo, D. J., Franklin, C., Lawson, P., Lohmann, U., McFarquhar, G., Ulanowski, Z. and Van Tricht, K. (2017) Cirrus Clouds. *Meteorological Monographs*, **58**, 2.1–2.26. URL: http://journals.ametsoc.org/doi/10.1175/AMSMONOGRAPHS-D-16-0010.1.

Hofer, S., Hahn, L. C., Shaw, J. K., McGraw, Z. S., Bruno, O., Hellmuth, F., Pietschnig, M., Mostue, I. A., David, R. O., Carlsen, T. and Storelvmo, T. (2024) Realistic representation of mixed-phase clouds increases projected climate warming. *Communications Earth & Environment*, **5**, 390. URL: https://www.nature.com/articles/s43247-024-01524-2.

Huang, X., Field, P. R., Murray, B. J., Grosvenor, D. P., Van Den Heuvel, F. and Carslaw, K. S. (2025) Different responses of cold-air outbreak clouds to aerosol and ice production depending on cloud temperature. URL: https://egusphere.copernicus.org/preprints/2025/egusphere-2024-4070/.

Kedzuf, N. J., Chiu, J. C., Chandrasekar, V., Biswas, S., Joshil, S. S., Lu, Y., Van Leeuwen, P. J., Westbrook, C., Blanchard, Y. and O'Shea, S. (2021) Retrieving microphysical properties of concurrent pristine ice and snow using polarimetric radar observations. *Atmospheric Measurement Techniques*, **14**, 6885–6904. URL: https://amt.copernicus.org/articles/14/6885/2021/.

Kolstad, E. W., Bracegirdle, T. J. and Seierstad, I. A. (2009) Marine cold-air outbreaks in the North Atlantic: temporal distribution and associations with large-scale atmospheric circulation. *Climate Dynamics*, **33**, 187–197. URL: http://link.springer.com/10.1007/s00382-008-0431-5.

Korolev, A., Isaac, G. A., Cober, S. G., Strapp, J. W. and Hallett, J. (2003) Microphysical characterization of mixed-phase clouds. *Quarterly Journal of the Royal Meteorological Society*, **129**, 39–65. URL: https://rmets.onlinelibrary.wiley.com/doi/10.1256/qj.01.204.

Korolev, A., McFarquhar, G., Field, P. R., Franklin, C., Lawson, P., Wang, Z., Williams, E., Abel, S. J., Axisa, D., Borrmann, S., Crosier, J., Fugal, J., Krämer, M., Lohmann, U., Schlenczek, O., Schnaiter, M. and Wendisch, M. (2017) Mixed-Phase Clouds: Progress and Challenges. *Meteorological Monographs*, **58**, 5.1–5.50. URL: https://journals.ametsoc.org/doi/10.1175/AMSMONOGRAPHS-D-17-0001.1.

Korolev, A. and Milbrandt, J. (2022) How Are Mixed-Phase Clouds Mixed? *Geophysical Research Letters*, **49**, e2022GL099578. URL: https://agupubs.onlinelibrary.wiley.com/doi/10.1029/2022GL099578.

Korolev, A., Strapp, J. W., Isaac, G. A. and Emery, E. (2013) Improved Airborne Hot-Wire Measurements of Ice Water Content in Clouds. *Journal of Atmospheric and Oceanic Technology*, **30**, 2121–2131. URL: http://journals.ametsoc.org/doi/10.1175/JTECH-D-13-00007.1.

Korolev, A., Strapp, J. W., Isaac, G. A. and Nevzorov, A. N. (1998) The Nevzorov Airborne Hot-Wire LWC–TWC Probe: Principle of Operation and Performance Characteristics. *Journal of Atmospheric and Oceanic Technology*, **15**, 1495–1510. URL: http://journals.ametsoc.org/doi/10.1175/1520-0426(1998)015<1495:TNAHWL>2.0.CO;2.

Korolev, A. V. (2008) Rates of phase transformations in mixed-phase clouds. *Quarterly Journal of the Royal Meteorological Society*, **134**, 595–608. URL: https://rmets.onlinelibrary.wiley.com/doi/10.1002/qj.230.

Lance, S., Brock, C. A., Rogers, D. and Gordon, J. A. (2010) Water droplet calibration of the Cloud Droplet Probe (CDP) and in-flight performance in liquid, ice and mixed-phase clouds during ARCPAC. *Atmospheric Measurement Techniques*, **3**, 1683–1706. URL: https://amt.copernicus.org/articles/3/1683/2010/.

Lawson, R. P., O'Connor, D., Zmarzly, P., Weaver, K., Baker, B., Mo, Q. and Jonsson, H. (2006) The 2D-S (Stereo) Probe: Design and Preliminary Tests of a New Airborne, High-Speed, High-Resolution Particle Imaging Probe. *Journal of Atmospheric and Oceanic Technology*, **23**, 1462–1477. URL: http://journals.ametsoc.org/doi/10.1175/JTECH1927.1.

Pithan, F., Medeiros, B. and Mauritsen, T. (2014) Mixed-phase clouds cause climate model biases in Arctic wintertime temperature inversions. *Climate Dynamics*, **43**, 289–303. URL: http://link.springer.com/10.1007/s00382-013-1964-9.

Raif, E. N., Barr, S. L., Tarn, M. D., McQuaid, J. B., Daily, M. I., Abel, S. J., Barrett, P. A., Bower, K. N., Field, P. R., Carslaw, K. S. and Murray, B. J. (2024) High ice-nucleating particle concentrations associated with Arctic haze in springtime cold-air outbreaks. URL: https://egusphere.copernicus.org/preprints/2024/egusphere-2024-1502/.

Renfrew, I. A. and Moore, G. W. K. (1999) An Extreme Cold-Air Outbreak over the Labrador Sea: Roll Vortices and Air–Sea Interaction. *Monthly Weather Review*, **127**, 2379–2394. URL: http://journals.ametsoc.org/doi/10.1175/1520-0493(1999)127<2379:AECAOO>2.0.CO;2.

Smith, D. K., Renfrew, I. A., van den Heuvel, F., Lachlan-Cope, T., Crawford, I., Bower, K., Flynn, M., Evans, M. D., Abel, S. J. and Field, P. R. (2025) The impact of mixed-phase cloud processes on the modelling of Southern Ocean clouds - 'in prep'.

Sokol, A. B. and Storelvmo, T. (2024) The Spatial Heterogeneity of Cloud Phase Observed by Satellite. *Journal of Geophysical Research: Atmospheres*, **129**, e2023JD039751. URL: https://agupubs.onlinelibrary.wiley.com/doi/10.1029/2023JD039751.

Van Weverberg, K., Morcrette, C. J., Boutle, I., Furtado, K. and Field, P. R. (2021) A Bimodal Diagnostic Cloud Fraction Parameterization. Part I: Motivating Analysis and Scheme Description. *Monthly Weather Review*, **149**, 841–857. URL: https://journals.ametsoc.org/view/journals/mwre/149/3/MWR-D-20-0224.1.xml.

Walters, D., Baran, A. J., Boutle, I., Brooks, M., Earnshaw, P., Edwards, J., Furtado, K., Hill, P., Lock, A., Manners, J., Morcrette, C., Mulcahy, J., Sanchez, C., Smith, C., Stratton, R., Tennant, W., Tomassini, L., Van Weverberg, K., Vosper, S., Willett, M., Browse, J., Bushell, A., Carslaw, K., Dalvi, M., Essery, R., Gedney, N., Hardiman, S., Johnson, B., Johnson, C., Jones, A., Jones, C., Mann, G., Milton, S., Rumbold, H., Sellar, A., Ujiie, M., Whitall, M., Williams, K. and Zerroukat, M. (2019) The Met Office Unified Model Global Atmosphere 7.0/7.1 and JULES Global Land 7.0 configurations. *Geoscientific Model Development*, **12**, 1909–1963. URL: https://gmd.copernicus.org/articles/12/1909/2019/.

Wegener, A. (1911) *Thermodynamik der atmosphäre*.

Wilson, D. R., Bushell, A. C., Kerr-Munslow, A. M., Price, J. D. and Morcrette, C. J. (2008) PC2: A prognostic cloud fraction and condensation scheme. I: Scheme description. *Quarterly Journal of the Royal Meteorological Society*, **134**, 2093–2107. URL: https://rmets.onlinelibrary.wiley.com/doi/10.1002/qj.333.

Yang, F., Ovchinnikov, M. and Shaw, R. A. (2014) Microphysical consequences of the spatial distribution of ice nucleation in mixed-phase stratiform clouds. *Geophysical Research Letters*, **41**, 5280–5287. URL: https://agupubs.onlinelibrary.wiley.com/doi/10.1002/2014GL060657.

Zheng, X., Zhang, Y., Klein, S. A., Zhang, M., Zhang, Z., Deng, M., Tian, J., Terai, C. R., Geerts, B., Caldwell, P. and Bogenschutz, P. A. (2024) Using Satellite and ARM Observations to Evaluate Cold Air Outbreak Cloud Transitions in E3SM Global Storm-Resolving Simulations. *Geophysical Research Letters*, **51**, e2024GL109175. URL: https://agupubs.onlinelibrary.wiley.com/doi/10.1029/2024GL109175.